Acta Pharmaceutica Sinica B 2026;16(4):2357−2374

Chinese Pharmaceutical Association
Institute of Materia Medica, Chinese Academy of Medical Sciences

Acta Pharmaceutica Sinica B

www.elsevier.com/locate/apsb
www.sciencedirect.com

ORIGINAL ARTICLE

Aberrant astroglial Kir4.1 activation in the anterior cingulate cortex disrupts neuronal excitability and social behavior

Zhengmao Li[a,b,†], Yixuan Zhang[b,†], Yan Chen[a,†], Ying Zhang[b], Yunlong Pan[a], Kerui Wang[a], Chen Li[b], Xiangyu Zhao[b], Weikang Hu[a], Yifan Luo[b], Jiawen Cheng[a], Hongzhen Zhang[b], Kohji Fukunaga[c], Yankai Xia[d], Jiandong Jiang[b,e], Xiuxiu Liu[b,*], Feng Han[b,f,g,*], Yingmei Lu[a,d,*]

[a]*Department of Physiology, School of Basic Medical Sciences, Nanjing Medical University, Nanjing 211166, China*
[b]*Medical Basic Research Innovation Center for Cardiovascular and Cerebrovascular Diseases, Ministry of Education, Key Laboratory of Cardiovascular & Cerebrovascular Medicine, School of Pharmacy, Nanjing Medical University, Nanjing 211166, China*
[c]*Department of CNS Drug Innovation, Graduate School of Pharmaceutical Sciences, Tohoku University, Sendai 980-8578, Japan*
[d]*Key Laboratory of Modern Toxicology of Ministry of Education, Nanjing 211166, China*
[e]*State Key Laboratory of Bioactive Substance and Function of Natural Medicines, Institute of Materia Medica, Chinese Academy of Medical Sciences/Peking Union Medical College, Beijing 100050, China*
[f]*Jiangsu Province Innovation Center for Brain-Inspired Intelligence Technology, Nanjing 210029, China*
[g]*Northern Jiangsu Institute of Clinical Medicine, The Affiliated Huaian No.1 People's Hospital of Nanjing Medical University, Huaian 223300, China*

Received 23 June 2025; received in revised form 23 October 2025; accepted 8 December 2025

KEY WORDS

Autism spectrum disorder;
Glufosiante ammonium;
Offspring;
Anterior cingulate cortex;

Abstract Prenatal herbicide exposure is increasingly linked to neurodevelopmental disorders, yet effective pharmacological interventions remain lacking due to unclear pathogenic mechanisms. Here, we demonstrate that prenatal exposure to glufosinate ammonium (GLA), a widely used herbicide, triggers autism-like behaviors, including social deficits and repetitive grooming, in offspring mice. Whole-brain c-Fos mapping, *in vivo* calcium imaging, and patch-clamp recordings identified hypoactive pyramidal

*Corresponding authors.
E-mail addresses: lufx@njmu.edu.cn (Yingmei Lu), fenghan169@njmu.edu.cn (Feng Han), xiuxiuliu@njmu.edu.cn (Xiuxiu Liu).
†These authors made equal contributions to this work.

Peer review under the responsibility of Chinese Pharmaceutical Association and Institute of Materia Medica, Chinese Academy of Medical Sciences.

https://doi.org/10.1016/j.apsb.2026.01.029

Astrocyte;
Pyramidal neurons;
Inwardly rectifying potassium channel 4.1;
Desipramine

neurons in the anterior cingulate cortex (ACC) as the neural substrate of these behavioral deficits in prenatally GLA-exposed offspring mice. Mechanistically, transcriptomic and multi-omics analyses revealed that astrocyte activation in the ACC drove Kir4.1 potassium channel upregulation, which suppressed CaMKIIα^+ neuronal excitability *via* impaired astrocyte−neuron communication. Pharmacological inhibition of astroglial Kir4.1 not only restored neuronal activity but also rescued social deficits in GLA-exposed offspring, underscoring Kir4.1's pivotal role in ACC dysfunction. Our study uncovers a novel astrocyte−neuron axis underlying herbicide-induced neurodevelopmental impairments and identifies Kir4.1 as a therapeutic target for environmental factor-associated autism.

1. Introduction

Environmental toxins are increasingly recognized as key contributors to neurodevelopmental disorders, with growing epidemiological evidence linking prenatal pesticide exposure to autism spectrum disorder (ASD)[1-5]. ASD, characterized by social deficits and repetitive behaviors, arises from complex gene−environment interactions[6-8]. Notably, gestational exposure to heavy metals and herbicides significantly elevates ASD risk in offspring, yet the precise neural mechanisms remain elusive[9,10].

Among environmental triggers, the broad-spectrum herbicide glufosinate ammonium (GLA) poses a pressing public health concern due to its widespread contamination of food and water supplies[11,12]. Preclinical studies demonstrate that even low-dose GLA exposure induces autism-like behaviors in offspring, concomitant with disrupted neurogenesis and neuronal migration[5,13]. However, critical knowledge gaps persist: the specific brain circuits impaired by GLA are undefined, the role of non-neuronal cells (*e.g.*, astrocytes) in GLA-induced synaptic dysfunction is unexplored, and no targeted therapies exist for herbicide-associated neurodevelopmental deficits.

ASD represents a complex neurodevelopmental condition characterized by multifaceted cellular pathophysiology[14,15]. Emerging evidence has underscored the critical roles of neurons, astrocytes, microglia, and oligodendrocytes in the pathogenesis of ASD[16-19]. Notably, single-cell transcriptomic studies have revealed cell-type-specific molecular signatures in ASD brain[20,21]. Astrocytes orchestrate critical neurodevelopmental processes including synaptic pruning, neurotransmitter recycling, and maintenance of ionic homeostasis, all of which are perturbed in ASD[22,23]. However, the precise mechanisms governing neuron−astrocyte communication in ASD remain poorly understood, particularly in the context of environmental risk factors.

Here, we identify anterior cingulate cortex (ACC), a hub for social behavior regulation, as a vulnerable target of prenatal GLA exposure. Using a pharmacological strategy combined with fiber photometry recordings and electrophysiologic approaches, we uncover a novel astrocyte-dependent mechanism: GLA-triggered Kir4.1 potassium channel overexpression in reactive astrocytes suppresses CaMKIIα^+ neuronal excitability, driving social deficits. Importantly, pharmacological inhibition of Kir4.1 rescues both neuronal activity and behavior, nominating this channel as a druggable target for ASD intervention.

2. Materials and methods

2.1. Animals and GLA administration

Five-week-old C57BL/6 mice were procured from Shanghai Laboratory Animal Co., Ltd. (Shanghai, China) and subjected to at least one week of acclimatization prior to the commencement of experimental procedures. Then, the mice were housed in an environment maintained at a temperature of 22−23 °C, a relative humidity of 40%−60% and a 12-h light/dark cycle. Access to water and sustenance was unrestricted throughout the study. As shown in Fig. 1A, female mice were randomly assigned to two groups ($n = 10$ per group): one receiving 12 μg/mL GLA (CAS No. 77182-82-2, Sigma−Aldrich, Switzerland) *via* drinking water, and the other receiving normal drinking water as a control. The GLA solution was replenished every three days to ensure consistent dosing, in accordance with previous methodologies[5,24]. Following an 8-week treatment, each group was paired with normal male counterparts in a 1:2 ratio to promote mating. GLA administration continued until delivery. The vehicle group is C57BL/6 mice of the same age, born to dams fed with normal drinking water. Offspring were weaned on postnatal Day 21, separated according to their genders and rehoused in cages (5 mice per cage). The offspring in each group were split into the control group and the prenatal GLA exposure group (PGEO)[5,24]. We then measured the body weight, brain weight, and brain water content of the offspring mice. For Kir4.1 inhibition, Desipramine (DES, HY-B1272, MedChemExpress, USA) was diluted in PBS. All experiments were performed with 1 mmol/L desipramine based on previous studies[25,26]. All animal procedures were approved by the Institutional Animal Care and Use Committee of Nanjing Medical University (IACUC-2206004) and were performed following the Chinese National Institutes of Health Guide for the Care and Use of Laboratory Animals.

2.2. Behavioral tests

Mice aged 6 - 10 weeks were transported to the behavioral test room, and after one week of adaptation, tested for autism-like behaviors. Mice were divided into GLA-treated and vehicle-treated control groups, and their behaviors were videoed and analyzed by SMART v3.0.05 (Panlab, Harvard Apparatus). All work surfaces were disinfected with 75% ethanol prior to the experiment.

2.2.1. Three-chamber social test (TCST)

TCST was conducted in a three-chamber apparatus measuring 60 cm × 40 cm × 40 cm, with middle and side chambers spanning 20 cm in width, to analyze the social behaviors of mice[27]. During phase 1 (Habituation), the mice were introduced into the central chamber for a stay of 10 min, allowing them to freely explore the environment. In phase 2, a stranger mouse (S1) was placed inside one cage, while the other cage remained empty. A tested mouse was led into the central chamber, with its gates open to adjacent chambers. Subsequently, the mouse was permitted to freely navigate the three chambers for 10 min. In the evaluation of social novelty preference (phase 3), another stranger mouse (S2) was placed into the empty cage. A tested mouse was then freed to explore the chambers again for 10 min. The stranger mice were randomly selected for these experiments and had the same sex as the tested mice. The time for the test mouse in sniffing the unfamiliar mouse and the empty object was recorded.

2.2.2. Self-grooming behavior test

This test was conducted to analyze the stereotyped behaviors of mice that were placed in an open field box, with freedom to roam and explore for a period of 10 min[27]. The time each mouse spent grooming during this 10-min period was measured using a randomized double-blind method.

2.2.3. Y-maze test

This test was conducted to assess the spatial working memory of mice. Following the protocol described in a previous study[28], we considered three consecutive entries into each arm as an alternation. The discrimination index was calculated as Eq. (1):

$$\text{The discrimination index} = (\text{Actual alternations}/\text{Maximum alternations}) \times 100 \quad (1)$$

2.2.4. Novel object recognition test (NORT)

NORT was performed to check the abilities of mice to memorize and recognize[28]. During the training phase, two identical cylinder objects were placed inside a 50 cm × 50 cm × 45 cm box. Then, one mouse was permitted to explore for 5 min. After a 4-h interval, any one of the cuboid objects was replaced with a novel cuboid object, followed by a 5-min test. We recorded the time spent by the mouse in sniffing the familiar and novel objects to determine whether it exhibited an innate preference for novelty. The recognition ratio was defined as Eq. (2):

$$\text{The recognition ratio} = (\text{Sniffing time on the novel object})/(\text{Sniffing time on the familiar object} + \text{Sniffing time on the novel object}) \times 100 \quad (2)$$

2.2.5. Openfield test (OFT)

OFT was performed to evaluate anxiety-like behavior in a plastic cube box (40 cm × 40 cm)[28,29]. The mouse was first habituated to the test room, then placed in the center of a chamber measuring 40 cm × 40 cm, with the central zone positioned 10 cm away from the edge. A video camera recorded the movements of the mouse during a period of 10 min. The time spent in the center was utilized as an indicator of anxiety.

2.2.6. Elevated plus maze test (EPM)

Anxiety-like behaviors were also evaluated by EPM[28,29]. An apparatus with two open arms (30 cm × 5 cm) and two closed arms (30 cm × 5 cm × 14 cm) was set up approximately 60 cm above the ground. The mouse was situated in the central zone of the apparatus, with its head facing the opened arm, and was granted with 8 min for free exploration. Anxiety-like behaviors were assessed according to the time spent in the open arms.

2.2.7. Immunohistochemistry

Brain tissues were sliced into 40-μm-thick using a freezing microtome (Leica CM 1950), and then preserved in a cryoprotectant solution containing PBS (50%), glycol (30%), and glycerol (20%) as previously described[28]. Each slice was then rinsed three times with PBS (10 min per wash), permeabilized with 0.1% Triton X-100 for 15 min, and finally blocked with TSA for 1 h at room temperature, and exposed to primary antibodies, including c-Fos (1:300, CST#2250) for 48 h, and then with fluorescent secondary antibodies for 4 h. Following three washes with PBS, the slice was visualized using a confocal microscope (Zeiss LSM 800), and data were processed by ImageJ software (NIH, USA).

2.3. In vivo fiber photometry recordings

2.3.1. Surgeries and viral injects

Mice were anesthetized with isoflurane gas/oxygen mixture (2%). The rAAV2/9-CaMKIIα-GCaMP6(s) (BrainVTA, Co., Ltd. Wuhan, China, #PT-0110, 5.31E+12 vg/mL) were microinfused with a glass pipette at 200 nL per side and 50 nL/min through a stereotaxic device (RWD Life Science) at the following stereotaxic coordinates: ACC (AP: +0.86 mm, ML: ±0.5 mm; DV: − 2.25 mm). Relative to bregma, AP, ML and DV denoted anteroposterior, mediolateral and dorsoventral, respectively.

2.3.2. Fiber photometry

Following rAAV2/9-CaMKIIα-GCaMP6(s) virus injection, an optical fiber (125 μm O.D., 0.37 numerical aperture (NA); Inper, Hangzhou, China) was placed in a ceramic ferrule and implanted into the ACC (AP: +0.86 mm, ML: ±0.5 mm; DV: −2.25 mm). The mice were allowed to recover for at least one week before fiber-photometry recording. The calcium ion signals in pyramidal neurons within the ACC of the mouse brain were monitored during social interaction. Fluorescence emitted by GCaMP6(s) was captured using an Inper fiber photometry system under the illumination of a blue LED at 470 nm. The LED output intensity was maintained at 30 μW/mm^2. The signals ranging between 503 and 538 nm were recorded with an acquisition rate of 10 Hz. The fluorescence change ($\Delta F/F$) was determined using the mean signal value as baseline, which was acquired 1 s prior to the interaction[30].

2.4. Two-photon laser scanning microscopy (TPLSM) imaging in vivo

Under anesthesia *via* isoflurane, mice were prepared for *in vivo* transcranial TPLSM. For the examination of microvascular morphology and hemodynamics, a cranial window (2 mm in diameter) was implanted at coordinates 2 mm posterior and 1.5 mm lateral to bregma. Following this, each mouse's head was immobilized using a custom-made metal frame with a 1-cm inner diameter. Parameters, like cerebral blood vessel diameter, velocity, and flow, were imaged *in vivo* through craniotomy. After dura mater removal, a metal frame 1-cm in diameter with an attachable 4-mm

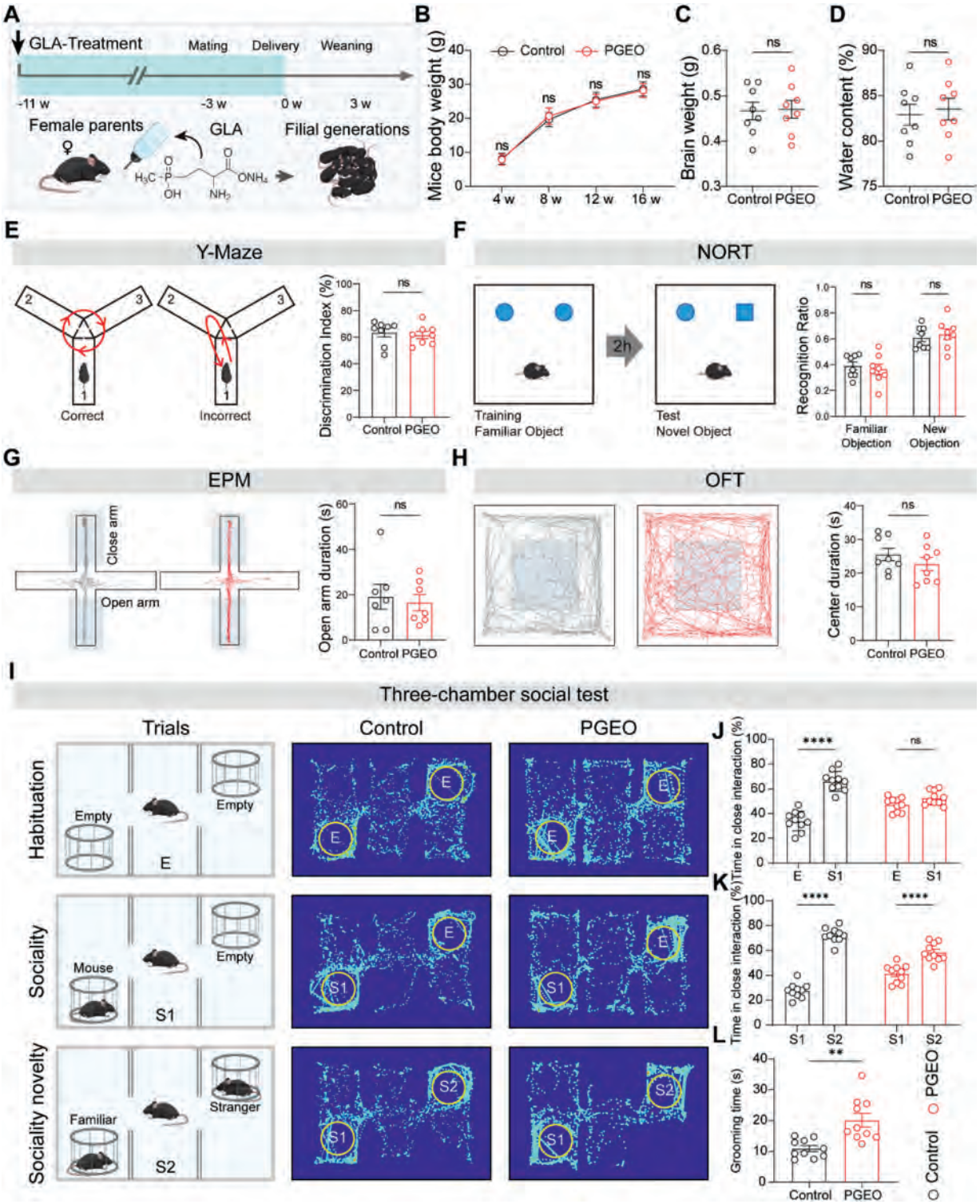

Figure 1 Prenatal GLA exposure induces autism-like symptoms in offspring mice. (A) Flow diagram of the study design. (B) Changes in body weight. Body weight of offspring mice was not influenced by GLA from 4 to 16 weeks (n = 20 Control mice, n = 20 PGEO mice). (C) Quantification of the brain weight (n = 8 Control mice, n = 8 PGEO mice). (D) Quantification of the cerebral water content (n = 8 Control mice, n = 8 PGEO mice). (E) Y-maze test (n = 8 Control mice, n = 8 PGEO mice). Discrimination index was not influenced by GLA. (F) Novel object recognition test (NORT) (n = 8 Control mice, n = 8 PGEO mice). The recognition ratio was not influenced by GLA. (G) Elevated plus maze (EPM) test (n = 7 Control mice, n = 7 PGEO mice). Time spent in the open arms was not influenced by GLA. (H) Open field test (OFT) (n = 8 Control mice, n = 8 PGEO mice). Time spent in the center was not influenced by GLA. (I) Schematic and heatmap of the three-chamber social test. (J) The time of interacting with the S1 mouse and the empty object in the sociability phase (phase 2) (n = 10 Control mice, n = 10 PGEO mice); S1: Strange mouse 1, E: Empty object. (K) The time of interacting with the S1 mouse and the S2 in the social novelty phase (phase

glass lid was fixed onto the skull. The gap between the brain surface and the cover glass was filled with saline. Stacked or single focal plane two-photon images were acquired using a two-photon laser scanning microscope (Carl Zeiss, LSM880 NLO) outfitted with an Airyscan Ultra High-Resolution System. Subsequently, a long-working-distance water immersion objective (25 ×, NA 1.05) was employed for the analysis of blood flow and microvascular morphology in the mouse brain cortex. For *in vivo* blood flow test, Texas Red Dextran solution (70 kDa, Sigma−Aldrich) was intravenously injected to label blood plasma. XYT and XYZ stacks captured images of 1024 × 1024-pixel resolution, with the former scanning at 2 μs/pixel speed and the latter at 4 μs/pixel speed across 300 μm depth. Velocity, diameter, flux, and line scan were assessed at a 10 μs/pixel scanning rate over a total of 2000 frames. Automated algorithms within MATLAB software processed all measurements concerning vessel diameters, blood velocities, and flux.

2.5. Electrophysiologic recordings

Mouse offspring aged two months were anesthetized. Brain tissues were immediately taken away and put into cold artificial cerebrospinal fluid. Then, the tissues containing ACC region were sectioned using a vibratome (Leica VT 1200S) and transferred into the normal artificial cerebrospinal fluid solution for electrophysiologic recording, as described previously[28].

2.5.1. Pyramidal neurons cell-attached recordings

Cell-attached recordings were selected to measure the APs of pyramidal neurons in the ACC. Whole-cell recordings were performed on ACC pyramidal neurons with a MultiClamp 700B amplifier, as described previously[27]. Glass micropipettes (4 to 6 MΩ) were used to establish tight seals at −70 mV for pyramidal neurons. APs, input resistance (Rin), membrane time constant (Tau) were recorded under current-clamp patch. Membrane capacitance (C_m) was obtained by dividing Tau by Rin.

2.5.2. Kir4.1 current isolation in astrocytes via whole-cell patch-clamp recordings

Astrocytes were distinguished from neurons based on their morphological features—small, oval somata (5−10 μm)—and their distinct electrophysiological signature, including an RMP of −80 mV, lower Rin, a linear I−V relationship, and an inability to generate action potentials with increasing depolarizing currents. Astrocytes were recorded in the whole-cell patch-clamp configuration under voltage-clamp mode, with a holding potential of −80 mV. Kir4.1 current was isolated by applying $BaCl_2$ (100 μmol/L; Sigma) and digitally subtracting the Ba^{2+}-sensitive component from the composite current recorded over a voltage range of −160 mV to +40 mV. Data were analyzed using MATLAB (MathWorks, Natick, MA, USA) and Clampfit 10 (Molecular Devices).

2.6. Transcriptional analysis

2.6.1. RNA isolation and library preparation

RNA was isolated from ACC tissues of both PGEO and control mice with TRIzol reagent (Invitrogen) according to the manufacturer's protocol. RNA concentration and purity were determined by a NanoDrop 2000 spectrophotometer (Thermo Scientific), and integrity was verified using an Agilent 2100 Bioanalyzer (Agilent Technologies). Following quality control, libraries were prepared from total RNA (RIN >7) using the VAHTS Universal V6 RNA-seq Library Prep Kit (Supporting Information Fig. S1A and S1B).

2.6.2. RNA sequencing and data analysis

The library was sequenced on Illumina Novaseq 6000, generating 150 bp paired-end reads. Reference transcriptome was sequenced in the ACC brain samples of all six PGEO and five control mice, resulting in 75.96 G CleanData after filtering sequences with a base quality lower than 20. The effective data volume of each sample ranged from 6.64 to 7.03 G, with a Q30 base distribution between 94.35% and 94.95%, and an average GC content of 50.13%. The genome alignment rate between the reads and the reference genome ranged from 98.27% to 98.5% for each sample. The logarithmic gene expression matrix was utilized for data analysis, with differential gene testing performed using Limma (3.58.1). GO and GSEA analyses were carried out using ClusterProfiler (3.18). The 3D scatter plot was visualized using plotly (4.10.4), heatmap using ComplexHeatmap (2.15.4), and the remaining plots using ggplot2 (3.5.0).

2.6.3. Single nucleus RNA sequencing data analysis

Single nucleus RNA sequencing data about the brain ACC of autism and control humans were obtained from the Sequence Read Archive (PRJNA434002). Cell ranger count was used to obtain raw counts matrix, features, and barcodes. Seurat 5.0 was used for quality control and identification of DEGs using FindMarkers (test use MAST). The astrocyte−pyramidal neuron crosstalk was visualized using ggsankey (0.0.9).

2.7. Real-time quantitative PCR

To validate RNA-seq-derived differentially expressed genes (DEGs), ACC brain tissues were dissected. Total RNA was extracted using RNAiso Plus (Takara) as previously described[31]. Following RNA extraction, 500 ng of RNA was reverse-transcribed into cDNA in a 20-μL reaction using the PrimeScript RT reagent Kit (Takara) with gene-specific primers. Subsequently, qRT-PCR was performed on a Mastercycler ep realplex (Eppendorf) using SYBR Premix Ex Taq (Takara) to quantify the mRNA levels of 23 DEGs. Reactions were run in 96-well plates under the following cycling conditions: 95 °C for 2 min, followed by 40 cycles of 95 °C for 15 s, 55 °C for 15 s, and 68 °C for 25 s. All primer sequences are provided in next section. Melting Curve Analysis: Conducted from 50 °C to 85 °C using default instrument settings. Data Analysis: Ct values were automatically calculated using commercial software. Relative

3) (n = 10 Control mice, n = 10 PGEO mice); S2: Strange mouse 2. (L) Quantification of the time in self-grooming during the 10-min free movement (n = 10 Control mice, n = 10 PGEO mice). Data are presented as mean ± SEM. $^{**}P < 0.01$, $^{****}P < 0.0001$ and ns = no significant difference, as determined by two-way analysis of variance (ANOVA) (B, F, J and K) and unpaired two-tailed Student's t test (C, D, E, G, H and L).

expression was normalized to β-actin/GAPDH and calculated using the $2^{-\Delta\Delta Ct} \pm$ s method.

Kir4.1:
Forward primer: GTCGGTCGCTAAGGTCTATTACA.
Reverse primer: GGCCGTCTTTCGTGAGGAC.
GAPDH:
Forward primer: AGGTCGGTGTGAACGGATTTG.
Reverse primer: GGGGTCGTTGATGGCAACA.

2.8. Plasmid constructs

The recombinant AAV (rAAV) plasmid, pAAV-GfaABC1D-EGFP-5′miR-30a-shRNA(*mKcnj10*)-3′miR-30a (Brain Case, Co., Ltd. Shenzhen, China, ≥5.00E+12 μg/mL), was constructed for astrocyte-specific knockdown of the *Kcnj10* gene. First, a short hairpin RNA (shRNA) targeting the mouse *Kcnj10* (*mKcnj10*) mRNA sequence was designed and embedded within a canonical murine miR-30a scaffold. This synthetic miRNA-shRNA cassette was then synthesized *in vitro* and cloned downstream of the enhanced green fluorescent protein (EGFP) reporter gene, into a pAAV backbone containing the human GfaABC1D promoter, a 681-bp fragment conferring specific expression in astrocytes. The control plasmid, rAAV-GfaABC1D-EGFP, was generated similarly but lacked the miRNA−shRNA insert. Both plasmids were packaged into AAV5 serotype capsids *via* triple transfection of HEK293T cells with the respective AAV *cis*-plasmid, the pAAV-RC5 rep/cap plasmid, and the pHelper plasmid. Seventy-two hours post-transfection, the viruses were harvested, purified *via* iodixanol density gradient centrifugation, and titered using quantitative PCR. We designed three shRNA sequences using RNAi designer online software (http://rnaidesigner.thermofisher.com/rnaiexpress/; Invitrogen) as indicated below:

BC-3014 shRNA1: GCAATGGCGCTACAAGCTTCTTTCAAGAGAAGAAGCTTGTAGCGCCATTGC.

BC-3015 shRNA2: GCTACAAGCTTCTGCTCTTCTTTCAAGAGAAGAAGAGCAGAAGCTTGTAGC.

BC-3016 shRNA3: GCTCTTCTCTGCAACCTTTGCTTCAAGAGAGCAAAGGTTGCAGAGAAGAGC.

The quantitative PCR detection results showed that the interference efficiencies were:

BC-3014: 92.48% (1−14.36/190.97).
BC-3015: 96.40% (1−6.87/190.97).
BC-3016: 94.47% (1−10.56/190.97).

Therefore, based on the detection results, shRNA from BC-3015 was ultimately selected to construct pAAV-GfaABC1D-EGFP-5′miR-30a-shRNA (*mKcnj10*) -3′miR-30a.

2.9. Statistical analysis

Statistical analyses were performed using GraphPad Prism 8. Data are presented as mean ± standard error of mean (SEM). For comparisons between two groups, an unpaired Student's *t*-test was used after confirming equal variance with an F-test. For comparisons involving multiple groups, one- or two-way ANOVA was applied, followed by Dunnett's, Sidak's, or Tukey's multiple comparisons test as appropriate. A P value < 0.05 was considered statistically significant ($^{*}P < 0.05$, $^{**}P < 0.01$, $^{***}P < 0.001$, $^{****}P < 0.0001$).

3. Results

3.1. Prenatal GLA exposure induces autism-like behaviors

To determine the neurodevelopmental impact of prenatal GLA exposure, we first assessed brain maturation and angioarchitecture in prenatal GLA-exposed offspring (PGEO) mice (Fig. 1A). Neither brain weight nor brain water content exhibited differences between the control and PGEO groups (Fig. 1B−D). We further utilized two-photon laser scanning microscopy (TPLSM) to analyze the angioarchitecture of capillaries[32,33], observing no significant differences in cerebral vessel diameter or blood flow velocity between groups (Supporting Information Fig. S2A−S2D).

Given the absence of gross structural or vascular deficits (Fig. S2E and S2F), we next evaluated behavioral phenotypes. We initially assessed cognitive function using the Y-maze test and the novel object recognition test (NORT). There were no significant differences in the discrimination index during the Y-maze test or in the recognition ratio during the NORT between two groups (Fig. 1E and F). Similarly, measures of anxiety-like behavior were unaffected, as evidenced by comparable time spent in the open arms of the elevated plus maze (EPM) and in the center zone of the open field test (OFT) between groups (Fig. 1G and H). These results suggest that prenatal GLA exposure does not impair general cognitive function or induce anxiety-like behaviors in offspring. As social deficits represent a core feature of ASD[5,27,34], we specifically examined social behaviors using the three-chamber sociability and social novelty tests. During the second phase (Phase 2), PGEO mice spent a comparable amount of time in sniffing the empty cage and unfamiliar mouse S1, unlike control mice which exhibited a significant preference for S1 (Fig. 1I and J). This lack of sociability preference indicates impaired social interaction in PGEO mice. In contrast, during the social novelty phase (Phase 3), PGEO mice, like controls, spent significantly more time sniffing the unfamiliar mouse S2 than they did the now-familiar mouse (S1) (Fig. 1I and K), demonstrating intact social novelty preference. Additionally, PGEO mice exhibited significantly increased time spent in self-grooming, indicative of elevated repetitive/stereotyped behavior (Fig. 1L).

Collectively, these findings establish PGEO mice as a model of herbicide-induced social dysfunction, mirroring ASD core symptoms, aligning with previous reports[5].

3.2. Prenatal GLA exposure specifically suppresses pyramidal neuronal activity in the ACC

Given accumulating evidence linking disrupted neuronal activity and functional connectivity in autism pathogenesis[6,35], we assessed neuronal activation patterns following social behavior testing. Following the sociability phase (Phase 2) of the three-chamber test, brain tissues were collected after a 30-min interval and processed for whole-brain c-Fos immunohistochemistry to map neuronal activity. Subsequent quantification of c-Fos-positive cells across sociability-related regions revealed a significant reduction in the ACC and hippocampus of PGEO mice compared to controls (Fig. 2A−C). The ACC and hippocampus, key limbic structures regulating instinctive

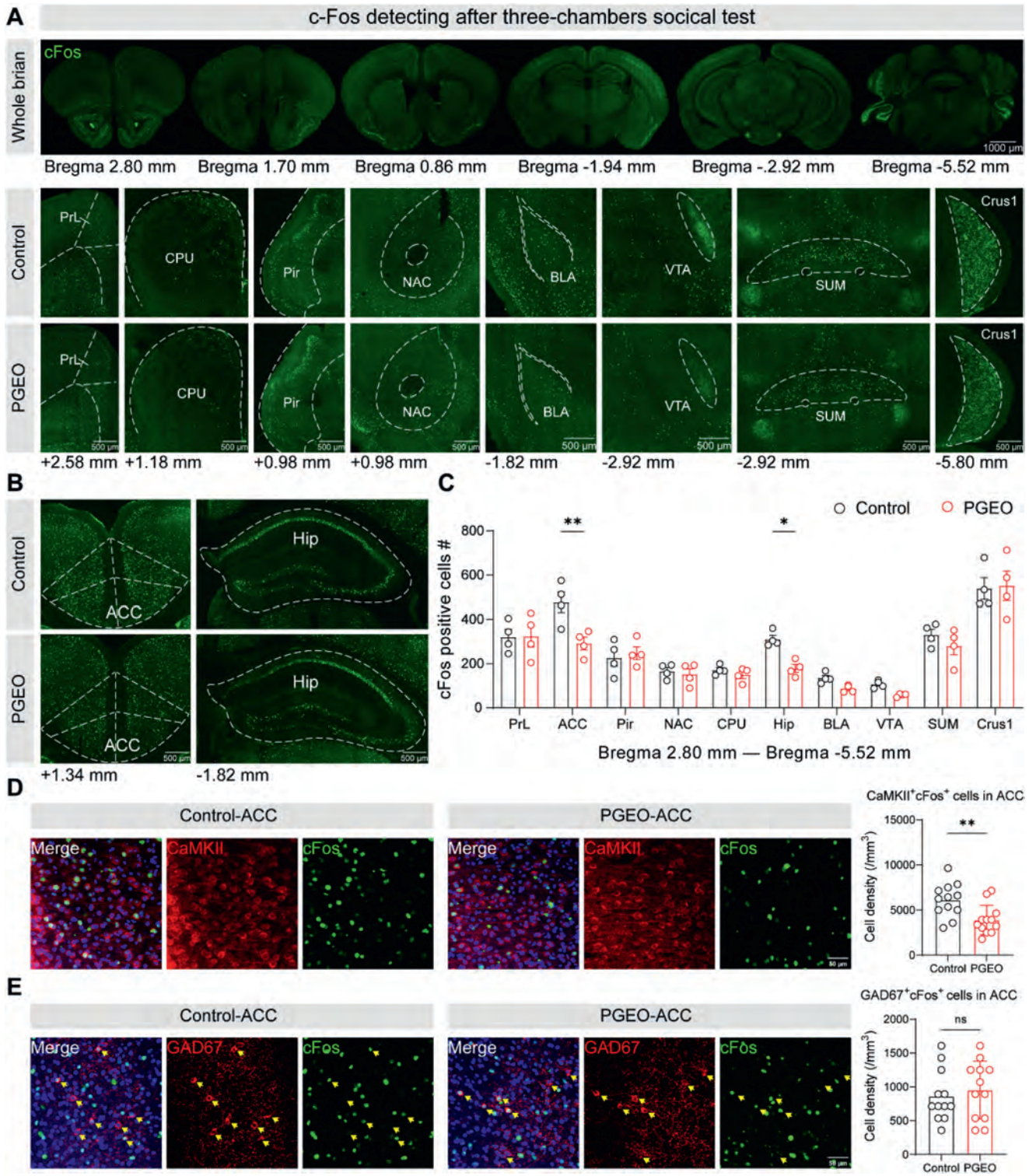

Figure 2 Autism-like behavior induced by GLA is related to the hypoactivity of pyramidal neurons in the ACC. (A) Representative brain slice tile scan confocal images and representative confocal images of the c-Fos (green) in the identified brain regions, which have been reported that associated with autism, in a coronal plane from 2.80 mm to −5.52 mm to the bregma after social interaction. Scale bar = 1000 and 500 μm, respectively. (B) Representative confocal images of the c-Fos (green) in the ACC and hippocampus after social interaction. Scale bar = 500 μm. (C) Quantitative results of c-Fos positive cells in 10 regions associated with autism (n = 4 Control mice, n = 4 PGEO mice). PrL: Prelimbic cortex; ACC: Anterior cingulate cortex; STR: Striatum; NAc: Nucleus accumbens; BLA: Basolateral amygdala; Hip: Hippocampus; VTA: Ventral tegmental area; SUM: Somatosensory cortex. (D) Colocalization and quantitative results of c-Fos and CaMKIIα which as markers in pyramidal neurons. (n = 12 slices from 4 Control mice, n = 12 slices from 4 PGEO mice, Scale bar = 50 μm). (E) Colocalization and quantitative results of c-Fos and GAD67 as markers in GABAergic neurons. (n = 12 slices from 4 Control mice, n = 12 slices from 4 PGEO mice, Scale bar = 50 μm). Data are presented as means ± SEM. *$P < 0.05$, **$P < 0.01$ and ns = no significant difference, as determined by two-way analysis of variance (ANOVA) (C) and unpaired two-tailed Student's t test (D, E).

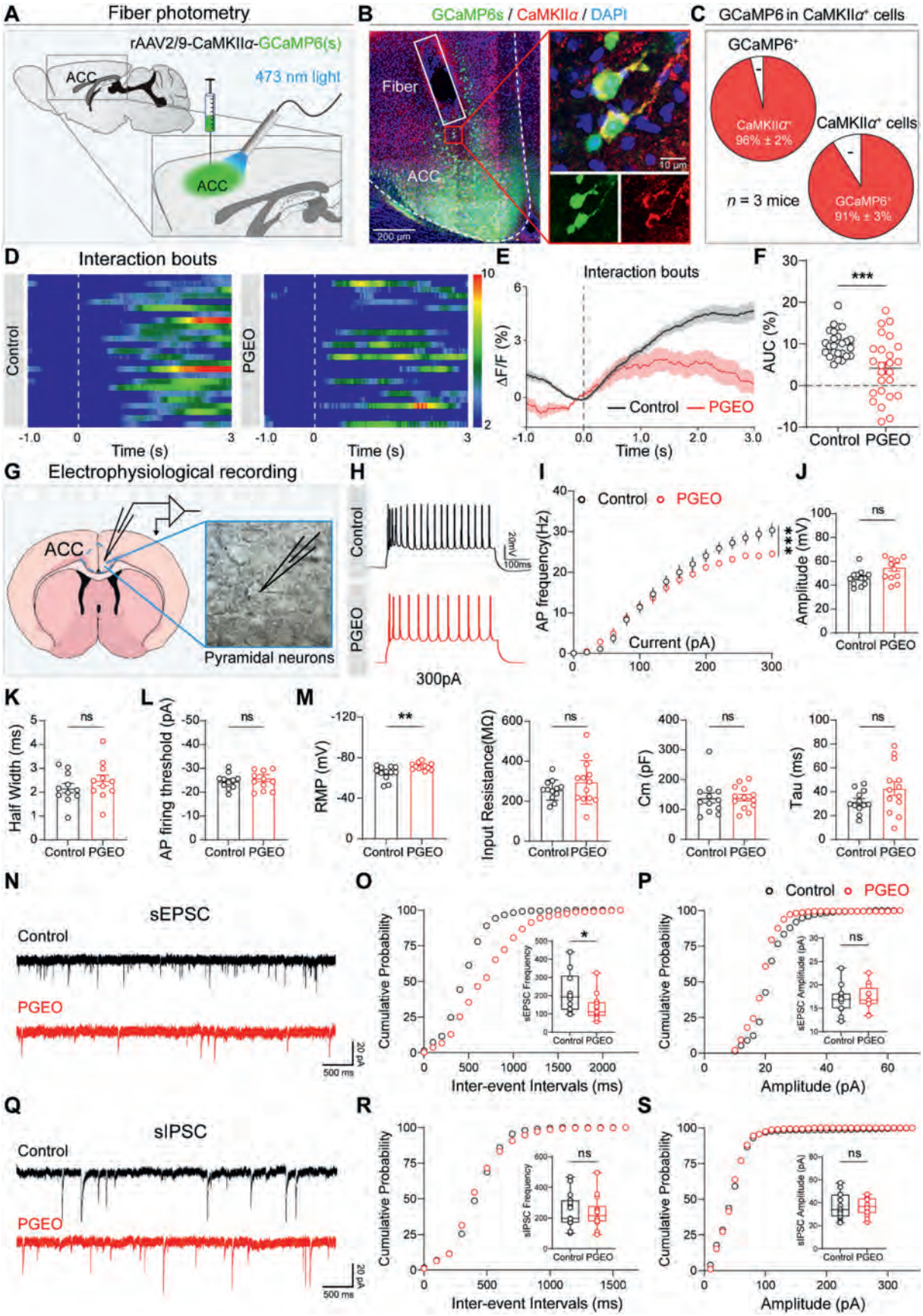
A
Fiber photometry
rAAV2/9-CaMKIIα-GCaMP6(s)
ACC
473 nm light
ACC
B
GCaMP6s / CaMKIIα / DAPI
Fiber
ACC
200 μm
10 μm
C
GCaMP6 in CaMKIIα⁺ cells
GCaMP6⁺
CaMKIIα⁺
96% ± 2%
CaMKIIα⁺ cells
GCaMP6⁺
91% ± 3%
n = 3 mice
D
Interaction bouts
Control
PGEO
Time (s)
E
Interaction bouts
ΔF/F (%)
Control
PGEO
Time (s)
F
AUC (%)
***
Control PGEO
G
Electrophysiological recording
ACC
Pyramidal neurons
H
Control
PGEO
20mV
100ms
300pA
I
Control
PGEO
AP frequency(Hz)
Current (pA)
***
J
Amplitude (mV)
ns
Control PGEO
K
Half Width (ms)
ns
Control PGEO
L
AP firing threshold (pA)
ns
Control PGEO
M
RMP (mV)
**
Input Resistance(MΩ)
ns
Cm (pF)
ns
Tau (ms)
ns
Control PGEO
N
sEPSC
Control
PGEO
20 pA
500 ms
O
Cumulative Probability
Inter-event Intervals (ms)
sEPSC Frequency
*
Control PGEO
P
Control
PGEO
Cumulative Probability
Amplitude (pA)
sEPSC Amplitude (pA)
ns
Control PGEO
Q
sIPSC
Control
PGEO
20 pA
500 ms
R
Cumulative Probability
Inter-event Intervals (ms)
sIPSC Frequency
ns
Control PGEO
S
Cumulative Probability
Amplitude (pA)
sIPSC Amplitude (pA)
ns
Control PGEO

and emotional behaviors, are functionally interconnected[36,37]. Notably, the ACC, as a key region regulating social behaviors, projects excitatory inputs to the hippocampal CA1 region that responds to feature-based contextual memory retrieval[38-40]. To determine the specific neuronal populations affected by prenatal GLA exposure within the ACC, we performed immunofluorescence co-localization analysis. This revealed a significant reduction in the number of neurons co-expressing CaMKIIα (a marker of excitatory pyramidal neurons) and c-Fos in the PGEO group, compared to the control group (Fig. 2D). However, no significant difference was observed in the co-localization of c-Fos with GAD67 (a marker of inhibitory GABAergic neurons) (Fig. 2E).

These results suggest that prenatal GLA exposure may specifically suppress the activity of pyramidal neurons in the ACC of offspring mice.

3.3. Prenatal GLA exposure inhibits ACC pyramidal neuronal firings

The observed reduction in c-Fos activation within CaMKIIα-positive neurons (Fig. 2D) prompted us to investigate whether this reflected neuronal loss in the ACC. Quantitative analysis using NEUN immunofluorescence, however, revealed no significant difference in total neuronal density between PGEO and control mice (Fig. S2G and S2H), indicating that the reduced activation was not attributable to cell loss. To directly test the link between ACC pyramidal neuron hypoactivity and the observed social deficits in PGEO mice, we employed *in vivo* fiber photometry in the ACC. An rAAV2/9-CaMKIIα-GCaMP(s) virus was injected into the ACC to express the calcium indicator GCaMP specifically in pyramidal neurons (Fig. 3A−C). During social interactions, PGEO mice exhibited a significant attenuation of calcium transient amplitudes in ACC pyramidal neurons compared to controls (Fig. 3D−F).

To characterize the intrinsic and synaptic properties underlying this hypoactivity, whole-cell patch-clamp recordings were conducted on ACC pyramidal neurons (Fig. 3G). Prenatal GLA exposure significantly reduced the frequency of action potentials (APs) evoked by depolarizing current steps in PGEO neurons (Fig. 3H and I). No significant differences were observed in action potential (AP) amplitude, AP half-width, firing threshold (Fig. 3J−L), as well as Rin, C_m, and Tau (Fig. 3M). Notably, the resting membrane potential (RMP) was significantly hyperpolarized in PGEO neurons (Fig. 3M). Next, we recorded the postsynaptic currents of pyramidal neurons in the ACC. The frequency of spontaneous excitatory postsynaptic currents (sEPSCs) was significantly decreased in PGEO ACC pyramidal neurons, without change in amplitude (Fig. 3N−P). Conversely, neither the frequency nor amplitude of spontaneous inhibitory postsynaptic currents (sIPSCs) was altered by prenatal GLA exposure (Fig. 3Q−S).

Collectively, these results demonstrate that prenatal GLA exposure induces functional hypoactivity in ACC pyramidal neurons *in vivo* and *ex vivo*, characterized by reduced AP firing, and a specific decrease in excitatory synaptic drive.

3.4. Activation of astrocytes in the ACC of PGEO mice

To investigate the mechanism underlying the decreased activity of pyramidal neurons in the ACC, RNA sequencing (RNA-seq) was conducted on ACC samples from six PGEO mice and five control mice (Fig. 4A). Following quality control and normalization, the expression data of 27,117 genes were obtained, and analyzed through dimensionality reduction by t-distributed stochastic neighbor embedding (t-SNE). The resultant three t-SNE components of each sample were projected into a 3D coordinate system, revealing a clear segregation in the transcriptional profile between the PGEO and control groups (Fig. 4B). Subsequent analysis revealed 3488 differentially expressed genes (DEGs) ($|\log2FC| > 0.1$, P value < 0.05) between the PGEO and control groups (Fig. 4C), some of which are autism-related and overexpressed notably. Gene ontology (GO) analysis showed these DEGs were particularly enriched in biological process (BP) terms related to wide-ranging glia cell functions, such as glia cell activation (Fig. 4D).

To further validate the RNA-Seq results, we conducted an immunofluorescence analysis on glial cells, including astrocytes and microglia within the ACC (Fig. 4E and Fig. S2I), which revealed significant increases in the densities of S100β^+ cells, GFAP $^+$ S100β^+ cells, and their proportion relative to the total S100β^+ cell population in the PGEO group (Fig. 4F−H). Moreover, correlation analysis showed a negative correlation between GFAP$^+$/S100β^+ cells and the number of CaMKIIα^+/cFos$^+$ cells in the ACC (Fig. 4I). Microglia also showed an increase in numbers and branches in the PGEO group (Fig. S2J−S2L). Based on RNA sequencing and microglial signature profiles, these microglial changes may represent an intermediate state between activation and silencing[41-44]. Given these results, we focused our subsequent investigations on exploring the connection between

Figure 3 The activity of ACC pyramidal neurons decreases during social interaction in offspring mice exposed to prenatal GLA. (A) Schematic of rAAV2/9-CaMKIIα-GCaMP6(s) injection into the ACC and fiber photometry recording during social interaction in the home-cage test. (B) Confirmation of fiber implantation sites and GCaMP6s (Green) virus infection in ACC pyramidal neurons (CaMKIIα, red). (C) Quantification of colocalization ratios: the percentage of GCaMP6-positive cells that are also CaMKIIα-positive, and the percentage of CaMKIIα-positive cells that are also GCaMP6-positive, in the ACC ($n = 3$ PGEO mice). (D) Heat map illustrating the calcium response ($\Delta F/F$, %) of ACC pyramidal neurons during social interaction. (E) The fiber photometry signal of ACC pyramidal neurons response to social interaction. Solid lines represent the mean value. Gray shadows represent ± SEM. (F) Area under the calcium photometry curve during social interaction (0−3 s). Control mice: $n = 25$ trials from 5 mice, PGEO mice: $n = 25$ trials from 5 mice. (G) Schematic representation of electrophysiological recordings of pyramidal neurons in the ACC. (H, I) Representative APs and quantification of the AP frequency by current injections from 0 to 300 pA (stepped by 20 pA) in ACC pyramidal neurons of Control and PGEO mice. (J−L) Quantification of the AP amplitude, half width, and firing threshold in ACC pyramidal neurons. (M) Quantification of RMP, Rin, Cm, and Tau of membrane properties in ACC pyramidal neurons under whole-cell recording. $n = 12$ cells from 3 Control mice, $n = 13$ cells from 3 PGEO mice. (N) Traces showing sEPSC recorded in Control and PGEO mice. (O, P) Cumulative probability plots summarizing the mean sEPSC inter-event intervals (O) and sEPSC amplitudes (P) in Control and PGEO mice. (Q) Traces showing sIPSC recorded in Control and PGEO mice. (R, S) Cumulative probability plots summarizing the mean sIPSC inter-event intervals (R) and sIPSC amplitudes (S) in Control and PGEO mice. The insets depict the average sEPSC and sIPSC amplitudes and frequencies. $n = 3$ Control mice, $n = 3$ PGEO mice. Data are presented as the mean ± SEM. $^*P < 0.05$, $^{**}P < 0.01$, $^{***}P < 0.001$ and ns = no significant difference, as determined by unpaired two-tailed Student's t test.

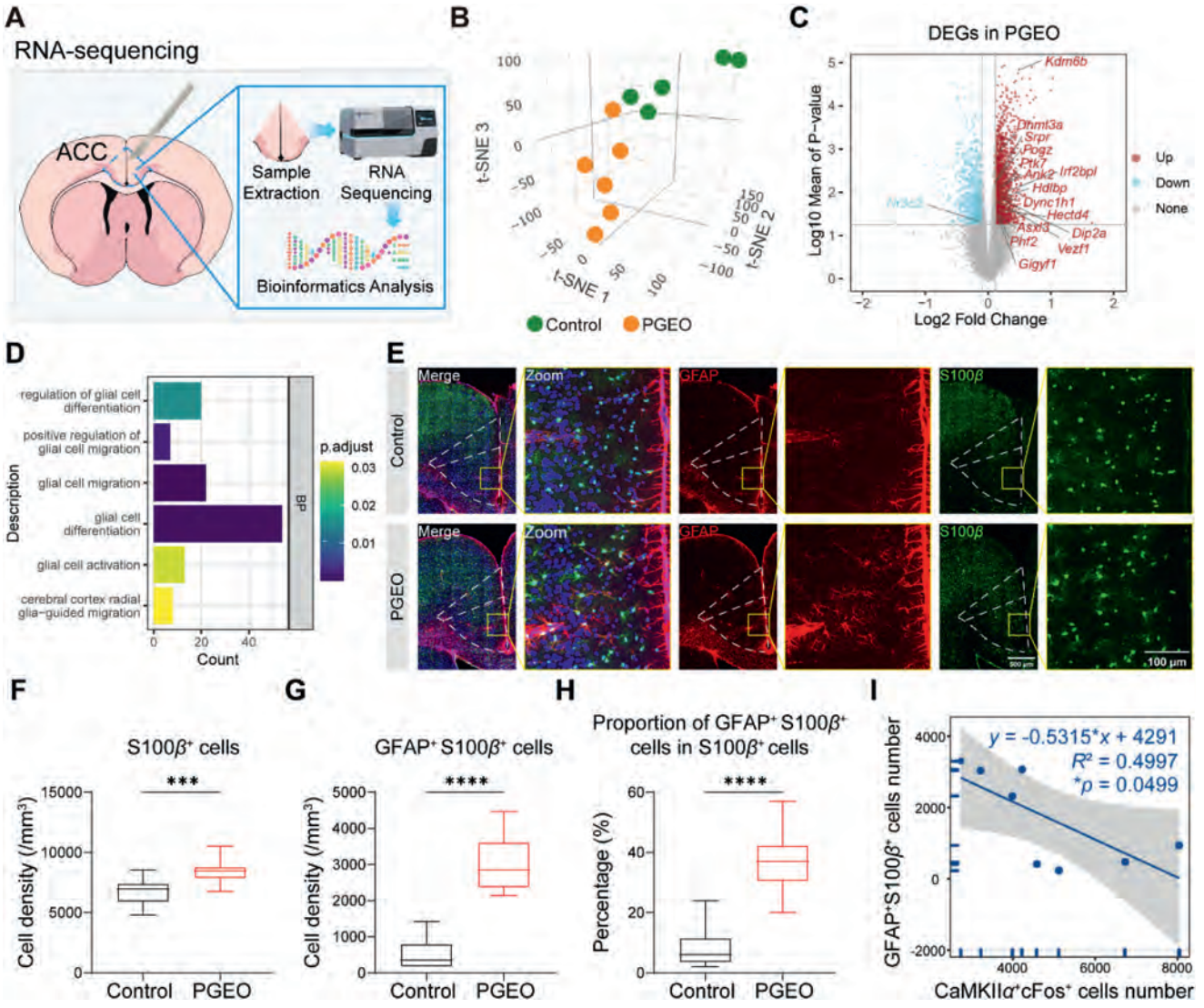

Figure 4 Astrocytes are activated in the ACC of offspring mice exposed to prenatal GLA. (A) The schematic diagram of RNA sequencing. (B) The three t-distributed stochastic neighbor embedding (t-SNE) components of each sample are visualized in a 3D coordinate system. (C) The volcano plot shows the differentially expressed genes (DEGs) between the control and PGEO groups. (D) Gene ontology (GO) enrichment analysis is conducted on the DEGs between the PGEO and the control groups, exhibiting various processes related to glial cells. (E) Representative confocal images of the S100β and GFAP immunofluorescence in the ACC. Scale bar, 500 μm (left); 100 μm (zoomed in, right). (F) The density of S100β^+ cells between the control and PGEO groups. (G) The density of GFAP $^+$ S100β^+ cells between the control and PGEO groups. (H) The percentage of GFAP $^+$ S100β^+ cells in all S100β^+ cells in the ACC between the control and PGEO groups. (I) The correlation analysis between GFAP $^+$ S100β^+ cells number and CaMKIIα^+cFos $^+$ cells in the ACC. $n = 12$ slices from 4 Control mice, $n = 12$ slices from 4 PGEO mice. Data are presented as the mean ± SEM. *$P < 0.05$, **$P < 0.001$ and ****$P < 0.0001$, as determined by unpaired two-tailed Student's t test (F–H).

astrocytic overactivity and neuronal hypoactivity, along with the underlying molecular mechanisms.

3.5. Kir4.1 augmentation underlies pyramidal neuron hypoactivity in the ACC

To investigate the molecular mechanism responsible for the hypoactivity of pyramidal neurons in the ACC of PGEO mice, we conducted in-depth analysis of RNA-seq data. Among previously identified DEGs between PGEO and control mice, 102 genes were selected for further characterization based on neuronal relevance. Of the 102 DEGs, 21 genes (20.59%) represent established autism risk genes[4] (Fig. 5A), potentially explaining autism-related molecular features in PGEO mice. Given that neuronal hypoactivity frequently involves ion channel function, we analyzed the GO items related to ion channels. Notably, all significantly enriched BP terms were specifically associated with potassium ion channels, including regulation of potassium channel transport, potassium channel complex components and voltage-gated potassium channel activity (Fig. 5B). Furthermore, we observed significant dysregulation of potassium channel-related genes following prenatal GLA exposure (Fig. 5C), providing a plausible molecular explanation for the altered firing frequency observed in the ACC pyramidal neurons.

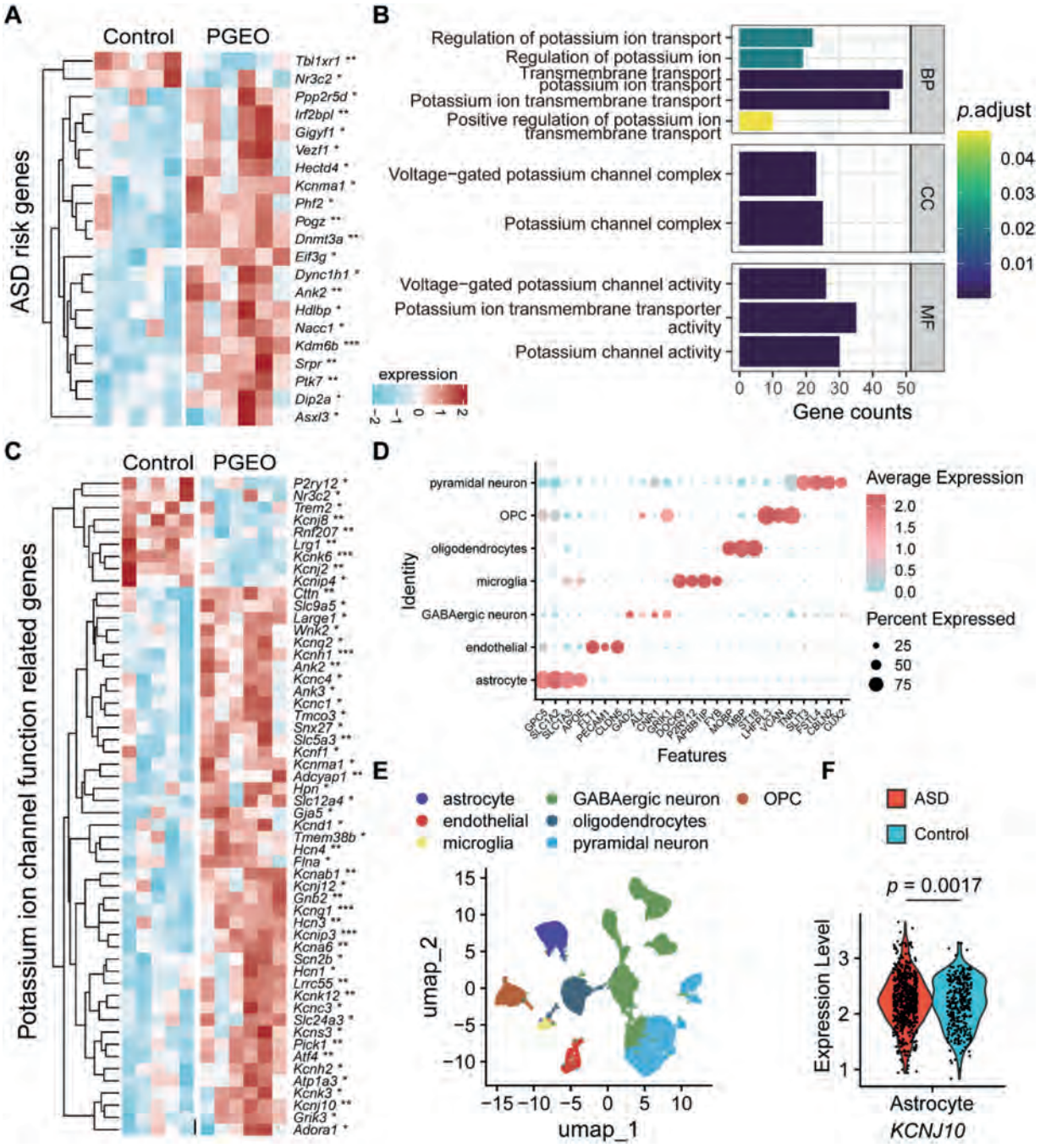

Figure 5 The augmentation of Kir4.1 is associated with the hypoactivity of pyramidal neurons in the ACC. (A) The gene expression heatmap displays the expression patterns of autism risk genes in the control and PGEO groups. (B) Gene ontology (GO) enrichment analysis is conducted on the DEGs from the PGEO group compared to the control group, exhibiting various terms related to potassium channel in the aspects of biological process (BP), cell component (CC), and molecular function (MF). (C) The gene expression heatmap represents the expression patterns of potassium channel-related genes in the control and PGEO groups. (D) The dot plot illustrates the average expression levels and expression percentage of cell annotation markers. (E) The UMAP visualization demonstrates the clusters of single nuclei in the ACC, with one color representing one cell type. (F) Violin plot of *KCNJ10* expression levels in astrocytes ($P = 0.0017$).

To determine whether potassium channel alterations in PGEO mice translate to human autism, we integrated a published snRNA-seq dataset[21] from the ACC of 9 autism patients and 9 non-autistic controls (total nuclei: 42,393). After uniform manifold approximation and projection (UMAP) for dimensionality reduction, cell types were annotated using accepted cell markers (Fig. 5D), yielding populations including pyramidal neurons, GABAergic neurons, astrocytes, microglia, endothelial cells, oligodendrocyte precursor cells (OPCs) and oligodendrocytes (Fig. 5E). Strikingly, analysis of potassium channel DEGs from PGEO mice within this human dataset revealed significantly elevated *KCNJ10* expression specifically in astrocytes of autism

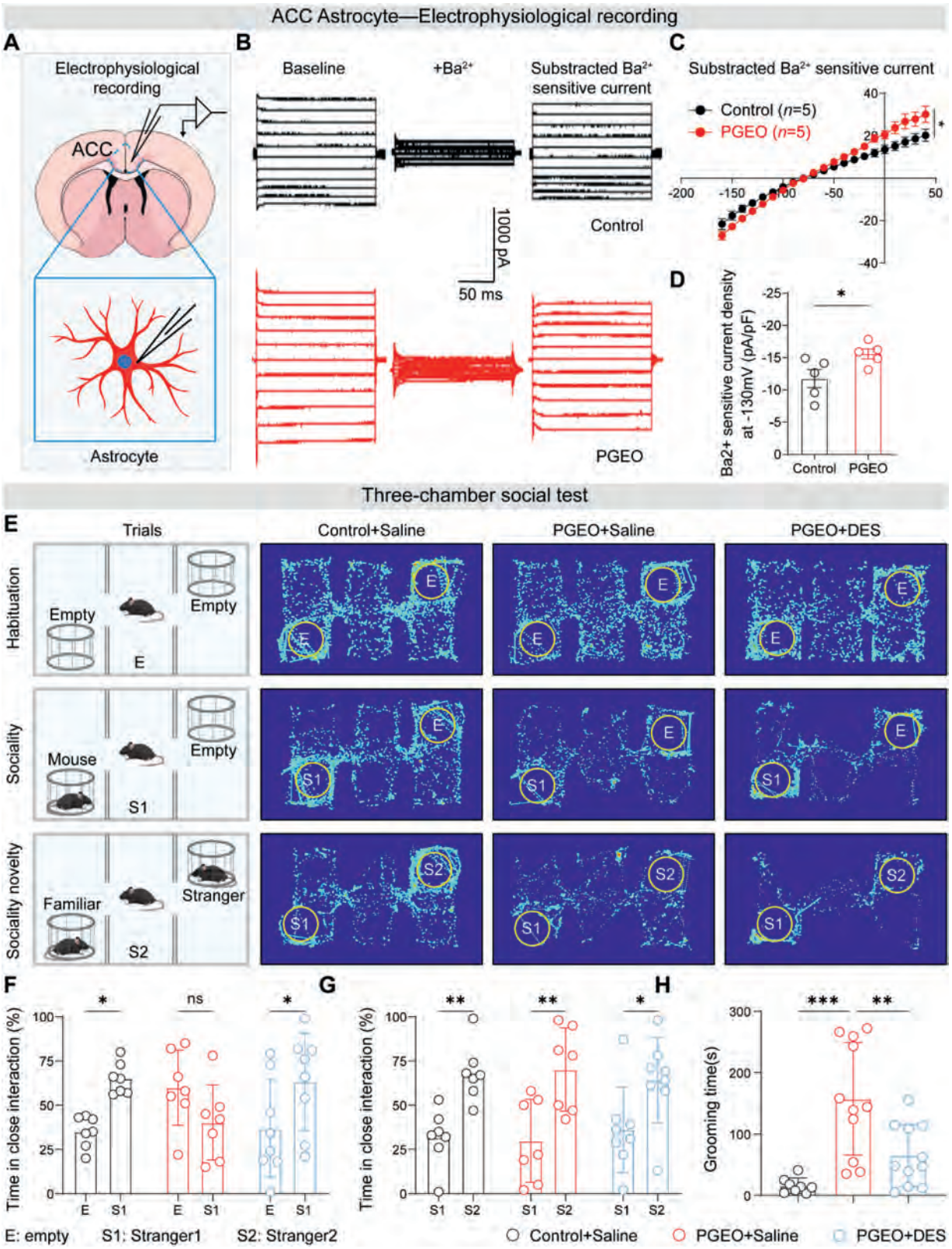

Figure 6 Pharmacological Kir4.1 inhibition ameliorates social deficits in PGEO mice. (A) The schematic diagram of whole-cell patch-clamp recordings on ACC astrocytes. (B) Representative traces showing linear I-V curve from a typical astrocyte before (left) and after (middle) Ba^{2+} perfusion under voltage steps (−130 to −30 mV, step by 10 mV, 150 ms duration, holding at −80 mV). Subtraction of the two led to Ba^{2+}-sensitive Kir current (right) in PGEO and Control mice. (C) Representative Ba^{2+} -sensitive Kir4.1 currents and related summary data for ACC astrocytes from PGEO mice ($n = 5$ cells from 3 mice) and Control mice ($n = 5$ cells from 3 mice). (D) Quantification of the Ba^{2+} -sensitive current density at −130 mV. (E) Schematic and heatmap of the three-chamber social tests among Control + Saline group, PGEO + Saline group

patients compared to controls (Fig. 5F). Given that *KCNJ10* encodes the astrocytic Kir4.1 potassium channel, we propose that the channel's dysregulation may underlie the observed pyramidal neuron hypoactivity.

3.6. *Kir4.1 inhibition ameliorates social deficits in PGEO mice*

To certify the hypothesis that abnormal Kir4.1 channel contributes to the hypoactivity of pyramidal neurons, we performed whole-cell patch-clamp recordings on ACC astrocytes in PGEO and control mice. We applied Ba^{2+} ($BaCl_2$, 100 μmol/L), a selective inhibitor of inwardly rectifying potassium channels (Kir), to isolate Kir4.1 current. Recordings revealed that there was a significant increase in Ba^{2+} sensitive currents in ACC astrocytes of PGEO mice compared to control mice (Fig. 6A−D). Consistent with this functional change, Kir4.1 protein expression was also significantly elevated in PGEO mice (Supporting Information Fig. S3A and S3B). These results suggest that the enhanced Kir4.1 currents are associated with hypoactivity of ACC pyramidal neurons under prenatal GLA exposure.

To determine whether Kir4.1 loss-of-function in the ACC could restore neuronal firing and ameliorate core autism-related phenotypes, we employed two distinct strategies. First, we delivered an astrocyte-targeting short hairpin RNA (shRNA) against *Kcnj10* (Kir4.1) into the ACC of PGEO mice using an adeno-associated virus (AAV2/5) under the control of the human GFAP promoter (GfaABC1D)[45] (Fig. S3C-Left). The specificity of astrocyte-targeted viral infection was verified by western blotting and immunostaining (Fig. S3C-Right). To characterize the intrinsic and synaptic properties underlying this modulation, we performed whole-cell patch-clamp recordings on pyramidal neurons in the ACC (Fig. S3D). Astrocyte-specific *Kir4.1* knockdown significantly restored the frequency of action potentials (APs) evoked by depolarizing current steps in ACC pyramidal neurons of PGEO mice (Fig. S3E). Notably, a significant depolarizing shift in RMPs was observed in neurons from AAV-sh(*Kcnj10*)-infected slices versus controls (Fig. S3I), while other electrophysiological parameters (AP amplitude, half-width, threshold, Rin, C_m, or Tau) were unaltered (Fig. S3F−S3I). These results suggest that astrocytic *Kir4.1* depletion specifically enhances excitability by increasing AP frequency and depolarizing RMP in a targeted manner. Consequently, AAV-mediated shRNA targeting *Kcnj10* [AAV-sh(*Kcnj10*)] markedly attenuated core autism-related phenotypes in PGEO mice, including a significant improvement in social ability during the social novelty phase of the three-chamber test (Fig. S3J and S3K). To further establish Kir4.1 as a druggable target, we employed the known Kir4.1 inhibitor desipramine and assessed its efficacy in ameliorating social deficits and repetitive stereotypies. In the three-chamber sociability test, PGEO mice treated with Desipramine spent significantly more time interacting with Stranger 1 (S1) during the sociability phase compared with PGEO mice treated with saline (Fig. 6E and F). Similarly, during the social novelty phase, Desipramine-treated PGEO mice showed a significantly increased preference for interacting with the novel Stranger 2 (S2) (Fig. 6G). In the self-grooming test, PGEO mice treated with Desipramine exhibited significantly longer grooming duration compared with control mice, and this phenotype was reversed by Desipramine treatment (Fig. 6H). Collectively, these results illustrate that astrocytic Kir4.1 loss-of-function or pharmacological inhibition of Kir4.1 channels alleviates core autism-related behavioral phenotypes in PGEO mice.

3.7. *Astrocytic Kir4.1 modulates pyramidal neuron activity via astrocyte−neuron crosstalk*

Based on the preceding findings, we hypothesize that Kir4.1 augmentation mediates pyramidal neuron hypoactivity *via* disrupted astrocyte−pyramidal neuron crosstalk. Here, we mapped the DEGs and their BPs of PGEO mice to the snRNA-seq data of human autism patients with ACC. Initially, we applied UMAP dimensionality reduction to astrocytes from autistic patients and controls, yielding distinct astrocyte subclusters (Fig. 7A). Notably, one subcluster (subcluster 2) was significantly enriched in autism samples and was therefore designated as autism-associated astrocytes (AAAs). Subsequent DEG analysis within these AAAs identified significant overlap with PGEO mouse DEGs (Fig. 7B). Gene set enrichment analysis (GSEA) of AAA DEGs indicated significant enrichment for functions including regulation of cell communication, cellular response to chemical stimuli, and monoatomic ion transmembrane transport (Fig. 7C). This profile aligns with previous GO analysis of PGEO ACC DEGs, suggesting conserved astrocytic transcriptional dysregulation between PGEO mice and human autism.

We next conducted an intersection analysis of the BPs in AAAs and PGEO mouse DEGs, identifying 221 shared BPs (Supporting Information Table S1). These processes were categorized into ten classes relevant to astrocyte−pyramidal neuron crosstalk, with synapse formation and function representing the predominant category (Fig. 7D). A heatmap visualizing the strength of crosstalk pathways highlighted significant dysregulation and specific affected mechanisms in autism (Fig. 7E). In PGEO, differentially expressed genes (DEGs) associated with glial cell processes, including *Kcnj10*, which encodes the inward-rectifying potassium channel Kir4.1, were also identified to participate in astrocyte−pyramidal neuron crosstalk (Fig. 7F). Given that administration of desipramine to PGEO mice potently rescued social deficits and decreased grooming duration (Fig. 6E−H), we further investigated whether this behavioral improvement was associated with the recovery of neuronal activity in the ACC. We performed patch-clamp electrophysiology to re-evaluate action potential firing of ACC pyramidal neurons following desipramine treatment. Patch-clamp recordings revealed that Desipramine (50 μmol/L) effectively restored action potential firing frequency in PGEO pyramidal neurons (Fig. 7G−I). Similarly, Desipramine administration normalized the hyperpolarized

and PGEO + DES group. (F) The time of interacting with the S1 mouse and the empty object in the sociability phase (phase 2) ($n = 7$ Control + Saline group, $n = 7$ PGEO + Saline group and $n = 8$ PGEO + DES group); S1: Strange mouse 1, E: Empty object. (G) The time of interacting with the S1 mouse and the S2 in the sociability novelty phase (phase 3) ($n = 7$ Control + Saline group, $n = 7$ PGEO + Saline group and $n = 8$ PGEO + DES group); S2: Strange mouse 2. (H) Quantification of the time in self-grooming during the 10-min free movement ($n = 8$ Control + Saline group, $n = 11$ PGEO + Saline group and $n = 11$ PGEO + DES group). Data are presented as means ± SEM. $^*P < 0.05$, $^{**}P < 0.01$, $^{***}P < 0.001$ and ns = no significant difference, as determined by unpaired two-tailed Student's *t* test (D) and two-way analysis of variance (ANOVA) (C and F−H).

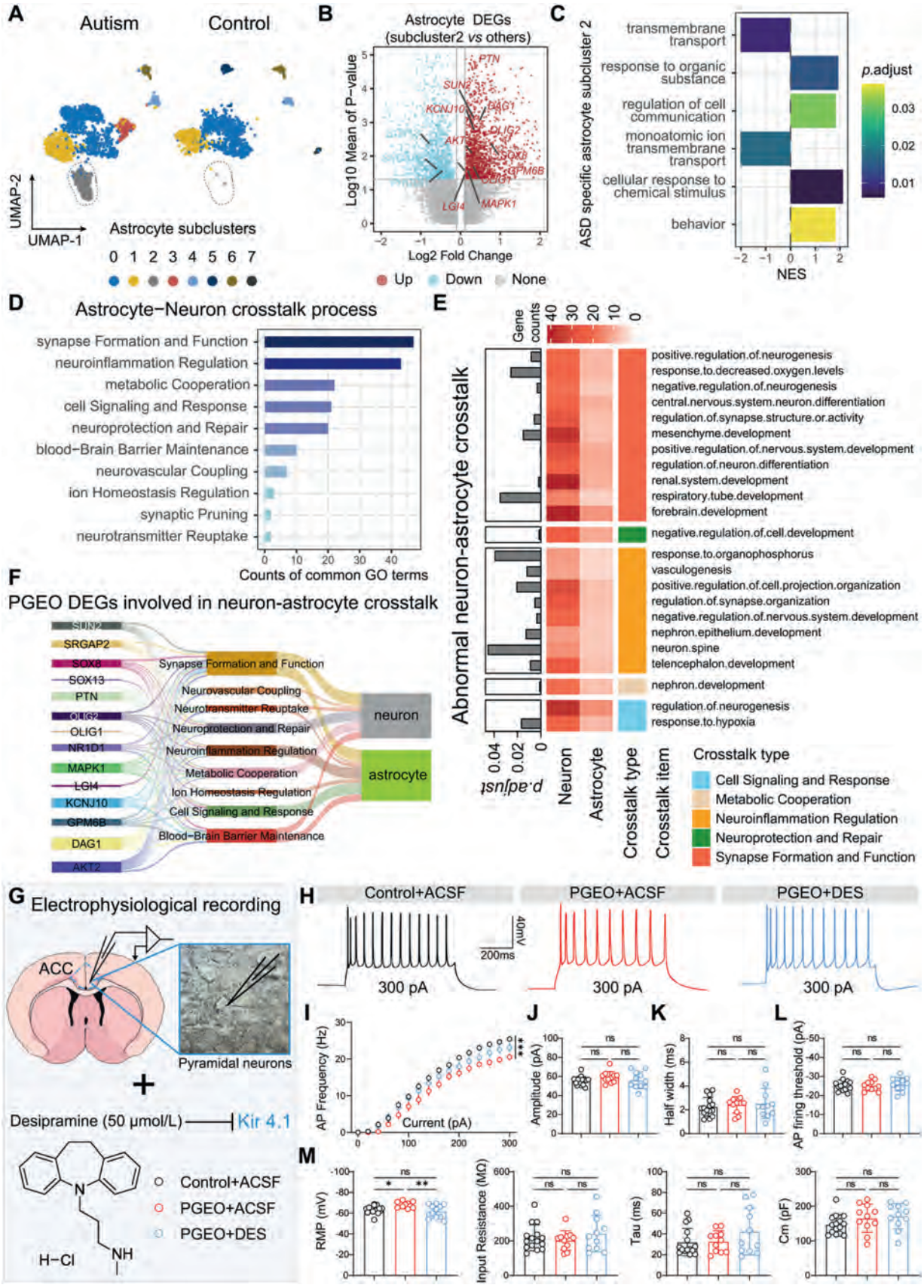

Figure 7 Astrocytic Kir4.1 modulates pyramidal neuron activity *via* astrocyte−neuron crosstalk. (A) The UMAP visualization demonstrates the subclusters of astrocytes in the ACC. (B) Volcano plot of DEGs between astrocyte subcluster 2 and other subclusters, with genes related to

RMPs in pyramidal neurons from PGEO groups, but had no significant effect on basal membrane properties (*e.g.*, Rin, C_m and Tau) of pyramidal neurons in either group (Fig. 7J−M).

Together, these data support a model where astrocytic Kir4.1 dysregulation disrupts astrocyte−pyramidal neuron crosstalk, particularly impacting synaptic processes, ultimately leading to neuronal hypoactivity and core behavioral phenotypes.

4. Discussion

The present study provides compelling evidence that prenatal exposure to GLA induces autism-like behaviors through a novel astrocyte-mediated mechanism involving Kir4.1 potassium channel dysregulation in the ACC. Our findings significantly advance the understanding of environmental risk factors in neurodevelopmental disorders and identify a potential therapeutic target for ASD intervention.

Our study demonstrated astrocyte-mediated dysregulation of neuronal excitability in the ACC of GLA-exposed offspring mice. The ACC maintains anatomical and functional connections with a wide range of regions that processing social information[46]. Moreover, dysfunction of inhibitory synapses within the ACC can trigger social deficits in animal models of neurodevelopmental disorders[47,48]. Besides neurons, a growing body of studies underscores the crucial role of astrocytes during pathological process of ASD[49-52]. We found astrocyte activation and GFAP overexpression in the ACC of PGEO mice. In alignment with our data, the postmortem examinations and animal models have reported alterations in the expression of key astrocytic markers, such as S100β, aquaporin 4 (AQP4), and Excitatory Amino Acid Transporter 1 (EAAT1), as well as increased presence of reactive astrocytes in the ASD pathological process[53-58].

How do activated astrocytes orchestrate these dynamic processes in neuronal excitability in GLA-exposed offspring mice? Our integrated multi-omics approach reveals broader pathophysiological implications. Transcriptomic convergence between PGEO mice and human ASD astrocytes suggests evolutionary conservation of glial potassium channel dysregulation in social impairment. Indeed, it is generally agreed that direct and indirect defects in K^+ channels are associated with the pathogenesis of ASD, and may disrupt neuronal network processes in multiple brain regions[59-61]. This alignment extends beyond Kir4.1 to include coordinated disruption of autism-associated gene networks regulating synaptic connectivity and ion homeostasis. ASD patients frequently carry KCNJ10 dominant activating mutations, implicating that astrocytic-dependent K^+ buffering may be a common mechanism leading to the core phenotype of ASD[62,63]. Such cross-species validation addresses a key limitation in environmental neurotoxicology studies and provides a mechanistic scaffold for understanding how transient gestational insults generate persistent circuit dysfunction. The ACC emerges as a vulnerability nexus where astrocyte−neuron metabolic coupling is hijacked by herbicide exposure, creating self-sustaining excitatory deficits *via* impaired potassium buffering.

AAV-mediated astrocytic *Kir4.1* knockdown, together with the pharmacological reversal of both behavioral and electrophysiological deficits *via* Kir4.1 inhibition, demonstrates that this channel is a therapeutically actionable target. Dysfunction in astrocyte-dependent potassium buffering may alter neuronal excitability and synaptic function, thereby contributing to autism phenotypes[64,65]. Consistent with our observations, a previous study demonstrated that elevated astrocytic Kir4.1 expression accelerates the clearance of ions released by neurons into the extracellular space[66]. This rapid clearance induces neuronal hyperpolarization, thereby promoting burst firing and depressive-like behaviors. In contrast, astrocyte-specific Kir4.1 loss-of-function in the LHb rescues depressive behaviors by reducing neuronal bursting[66]. Aberrant synaptic transmission and dendritic spines in neurons play a key role in ASD, while synaptic activity is controlled by astrocytes[67,68]. Desipramine-mediated rescue of social deficits and repetitive behaviors, alongside restoration of pyramidal neuron firing, demonstrates that developmental synaptic impairments remain modifiable post-insult. This repurposing of desipramine moves beyond correlation to directly establish a causal role for astrocytic Kir4.1 in circuit dysfunction. Metabolic coupling between neurons and astrocytes has been proven essential for supporting brain function[69-71]. Consistent with that astrocytic Kir4.1 plays a primary regulatory role in pathological process of GLA-induced ASD, we observed that the frequency of spontaneous excitatory postsynaptic currents decreased in the same context. Moreover, the dissociation between rescued social behaviors and unaffected anxiety/cognition highlights the circuit-specificity of this intervention, a crucial consideration for targeted ASD therapeutics.

Several critical questions remain unresolved. Neurons and glial cells are interdependent across multiple aspects of biological development and function[72], yet the mechanism by which abnormalities in glial cell migration and differentiation affect the neuronal system remains to be further elucidated. The temporal dynamics of astrocytic Kir4.1 dysregulation whether it initiates during prenatal exposure or amplifies postnatally require longitudinal investigation. Second, the specific contribution of Kir4.1 relative to other potassium channels and broader astrocyte functions remains to be clarified. Third, it is important to explore whether GLA exposure affects brain regions beyond the anterior cingulate cortex or influences behavioral domains not examined in this study. Potential sex differences in astrocytic responses to GLA must be evaluated given male-predominant ASD

glial cell activation labeled in the plot. (C) Gene set enrichment analysis (GSEA) displays BPs enriched in astrocyte subcluster 2. NES: normalized enrichment score. An NES score greater than 0 indicates that this BP is enhanced, while a score less than 0 indicates the opposite. (D) Ten types of astrocyte−neuron crosstalk. (E) Strength heatmaps of significant categories of astrocyte−pyramidal neuron crosstalk and specific processes between neurons and astrocyte subcluster 2. (F) Sankey plot indicates *KCNJ10* mediates crosstalk between astrocytes and pyramidal neurons by participating in various BPs. (G) Schematic representation of electrophysiological recordings of pyramidal neurons in the ACC. (H, I) Representative APs and quantification of the AP frequency by current injections from 0 to 300 pA (stepped by 20 pA) in ACC pyramidal neurons of Control and PGEO mice treated with ACSF or 50 μmol/L desipramine. (J−L) Quantification of the AP amplitude, half width and threshold in ACC pyramidal neurons. (M) Quantification of RMP, Rin, Tau, and Cm of membrane properties in ACC pyramidal neurons under patch-clamp recording. $n = 15$ cells from 3 Control mice treated with ACSF, $n = 11$ cells from 3 PGEO mice treated with ACSF, $n = 11$ cells from 3 PGEO mice treated with desipramine. Data are presented as the mean ± SEM. $^*P < 0.05$ and ns = no significant difference, as determined by one-way analysis of variance (ANOVA) (J−M) and two-way analysis of variance (ANOVA) (I).

epidemiology[73,74]. Technical innovations combining astrocyte-specific Kir4.1 manipulation with *in vivo* potassium imaging will help dissect the spatial consequences of channel dysfunction across the ACC.

5. Conclusions

This work redefines environmental neurotoxicity paradigms by demonstrating that herbicides reprogram astrocytic function rather than merely damaging neurons. We position Kir4.1 as a mechanism-based therapeutic target with disease-modifying potential. Future efforts should develop brain-penetrant Kir4.1 inhibitors and explore their synergy with neuromodulatory approaches for environmentally triggered neurodevelopmental disorders.

Acknowledgments

This research was supported by the National Innovation of Science and Technology2030, STI2030-Major Projects 2021ZD0204002 (China); The National Key Research and Development Program of China (W2411078); The National Natural Science Foundation of China (82304469, 82204352); Basic Research Program of Jiangsu, Jiangsu Province Innovation Center for Brain-Inspired Intelligence Technology (BM2024001, China). The Jiangsu Funding Program for Excellent Postdoctoral Talent (2023ZB301, 2022ZB431, China).

Author contributions

Feng Han, Yingmei Lu, Xiuxiu Liu and Yankai Xia initialized and conceived the overall study. Feng Han and Yingmei Lu supervised the project. Zhengmao Li and Yixuan Zhang: Conducting all the experiments. Ying Zhang, Kerui Wang and Chen Li: Performing the electrophysiological recording. Yan Chen, Yunlong Pan and Jiawen Cheng: performing the RNA-Seq data analysis. Xiangyu Zhao, Weikang Hu and Yifan Luo: Assisting the animal behavior tests. Hongzhen Zhang: Assisting the immunofluorescence experiment. Feng Han, Jiandong Jiang and Kohji Fukunaga contributed to the experiments design and the initial draft. Xiuxiu Liu and Zhengmao Li made critical revision for the manuscript.

Conflicts of interest

The authors declare no conflicts of interest.

Data availability

The RNA-seq data of this study are available from the authors upon request and delivery through Science Data Bank (https://www.scidb.cn/en).

Appendix A. Supporting information

Supporting information to this article can be found online at https://doi.org/10.1016/j.apsb.2026.01.029.

References

1. Bemanalizadeh M, Khoshhali M, Goli P, Abdollahpour I, Kelishadi R. Parental occupational exposure and neurodevelopmental disorders in offspring: a systematic review and meta-analysis. *Curr Environ Health Rep* 2022;**9**:406−22.
2. Dickerson AS, Frndak S, DeSantiago M, Mohan A, Smith GS. Environmental exposure disparities and neurodevelopmental risk: a review. *Curr Environ Health Rep* 2023;**10**:73−83.
3. Maglio LE, Noriega-Prieto JA, Maroto IB, Martin-Cortecero J, Munoz-Callejas A, Callejo-Mostoles M, et al. IGF-1 facilitates extinction of conditioned fear. *eLife* 2021;**10**:e67267.
4. Satterstrom FK, Kosmicki JA, Wang J, Breen MS, De Rubeis S, An JY, et al. Large-scale exome sequencing study implicates both developmental and functional changes in the neurobiology of autism. *Cell* 2020;**180**:568−84.
5. Dong T, Guan Q, Hu W, Zhang M, Zhang Y, Chen M, et al. Prenatal exposure to glufosinate ammonium disturbs gut microbiome and induces behavioral abnormalities in mice. *J Hazard Mater* 2020;**389**:122152.
6. Jiang CC, Lin LS, Long S, Ke XY, Fukunaga K, Lu YM, et al. Signalling pathways in autism spectrum disorder: mechanisms and therapeutic implications. *Signal Transduct Targeted Ther* 2022;**7**:229.
7. Zhuang H, Liang Z, Ma G, Qureshi A, Ran X, Feng C, et al. Autism spectrum disorder: pathogenesis, biomarker, and intervention therapy. *MedComm* 2024;**5**:e497.
8. Zhang J, Cai F, Lu R, Xing X, Xu L, Wu K, et al. CNTNAP2 intracellular domain (CICD) generated by gamma-secretase cleavage improves autism-related behaviors. *Signal Transduct Targeted Ther* 2023;**8**:219.
9. Liew Z, Meng Q, Yan Q, Schullehner J, Hansen B, Kristiansen SM, et al. Association between estimated geocoded residential maternal exposure to lithium in drinking water and risk for autism spectrum disorder in offspring in Denmark. *JAMA Pediatr* 2023;**177**:617−24.
10. Xu Y, Yang X, Chen D, Xu Y, Lan L, Zhao S, et al. Maternal exposure to pesticides and autism or attention-deficit/hyperactivity disorders in offspring: a meta-analysis. *Chemosphere* 2023;**313**:137459.
11. Ashley-Martin J, Huang R, MacPherson S, Brion O, Owen J, Gaudreau E, et al. Urinary concentrations and determinants of glyphosate and glufosinate in pregnant Canadian participants in the MIREC study. *Environ Res* 2023;**217**:114842.
12. Suciu N, Russo E, Calliera M, Luciani GP, Trevisan M, Capri E. Glyphosate, glufosinate ammonium, and AMPA occurrences and sources in groundwater of hilly vineyards. *Sci Total Environ* 2023;**866**:161171.
13. Herzine A, Laugeray A, Feat J, Menuet A, Quesniaux V, Richard O, et al. Perinatal exposure to glufosinate ammonium herbicide impairs neurogenesis and neuroblast migration through cytoskeleton destabilization. *Front Cell Neurosci* 2016;**10**:191.
14. Wamsley B, Bicks L, Cheng Y, Kawaguchi R, Quintero D, Margolis M, et al. Molecular cascades and cell type-specific signatures in ASD revealed by single-cell genomics. *Science* 2024;**384**. eadh2602.
15. Gandal MJ, Haney JR, Wamsley B, Yap CX, Parhami S, Emani PS, et al. Broad transcriptomic dysregulation occurs across the cerebral cortex in ASD. *Nature* 2022;**611**:532−9.
16. Cano A, Santos D, Beltrao-Braga PCB. The interplay of astrocytes and neurons in autism spectrum disorder. *Adv Neurobiol* 2024;**39**:269−84.
17. Luo Y, Wang Z. The impact of microglia on neurodevelopment and brain function in autism. *Biomedicines* 2024;**12**:210.
18. Ramesh V, Tsoukala E, Kougianou I, Kozic Z, Burr K, Viswanath B, et al. The Fragile X messenger ribonucleoprotein 1 regulates the morphology and maturation of human and rat oligodendrocytes. *Glia* 2025;**73**:1203−20.
19. Sohal VS, Rubenstein JLR. Excitation-inhibition balance as a framework for investigating mechanisms in neuropsychiatric disorders. *Mol Psychiatr* 2019;**24**:1248−57.
20. Tai DJC, Razaz P, Erdin S, Gao D, Wang J, Nuttle X, et al. Tissue- and cell-type-specific molecular and functional signatures of 16p11.2 reciprocal genomic disorder across mouse brain and human neuronal models. *Am J Hum Genet* 2022;**109**:1789−813.
21. Velmeshev D, Schirmer L, Jung D, Haeussler M, Perez Y, Mayer S, et al. Single-cell genomics identifies cell type-specific molecular changes in autism. *Science* 2019;**364**:685−9.

22. Wang J, Gao Y, Xiao L, Lin Y, Huang L, Chen J, et al. Increased NMDARs in neurons and glutamine synthetase in astrocytes underlying autistic-like behaviors of *Gabrb1*$^{-/-}$ mice. *iScience* 2023;**26**:107476.
23. Wang Q, Kong Y, Wu DY, Liu JH, Jie W, You QL, et al. Impaired calcium signaling in astrocytes modulates autism spectrum disorder-like behaviors in mice. *Nat Commun* 2021;**12**:3321.
24. Laugeray A, Herzine A, Perche O, Hebert B, Aguillon-Naury M, Richard O, et al. Pre- and postnatal exposure to low dose glufosinate ammonium induces autism-like phenotypes in mice. *Front Behav Neurosci* 2014;**8**:390.
25. Tang X, Schmidt TM, Perez-Leighton CE, Kofuji P. Inwardly rectifying potassium channel Kir4.1 is responsible for the native inward potassium conductance of satellite glial cells in sensory ganglia. *Neuroscience* 2010;**166**:397−407.
26. Li X, Li Q, Xu L, Ma Z, Shi Y, Zhang X, et al. Involvement of Kir4.1 in pain insensitivity of the BTBR mouse model of autism spectrum disorder. *Biochim Biophys Acta Mol Basis Dis* 2023;**1869**:166700.
27. Luo YF, Lu L, Song HY, Xu H, Zheng ZW, Wu ZY, et al. Divergent projections of the prelimbic cortex mediate autism- and anxiety-like behaviors. *Mol Psychiatr* 2023;**28**:2343−54.
28. Tan C, Lu NN, Wang CK, Chen DY, Sun NH, Lyu H, et al. Endothelium-derived semaphorin 3G regulates hippocampal synaptic structure and plasticity *via* neuropilin-2/plexinA4. *Neuron* 2019;**101**:920−37.
29. Han X, Xu T, Ding C, Wang D, Yao G, Chen H, et al. Neuronal NR4A1 deficiency drives complement-coordinated synaptic stripping by microglia in a mouse model of lupus. *Signal Transduct Targeted Ther* 2022;**7**:50.
30. Peng X, Mao Y, Tai Y, Luo B, Dai Q, Wang X, et al. Characterization of anxiety-like behaviors and neural circuitry following chronic moderate noise exposure in mice. *Environ Health Perspect* 2023;**131**:107004.
31. Li ZM, Liu XX, Li C, Wei ZC, Shi Y, Song HY, et al. Decreased synapse-associated proteins are associated with the onset of epileptic memory impairment in endothelial CDK5-deficient mice. *MedComm* 2022;**3**:e128.
32. Garic D, McKinstry RC, Rutsohn J, Slomowitz R, Wolff J, MacIntyre LC, et al. Enlarged perivascular spaces in infancy and autism diagnosis, cerebrospinal fluid volume, and later sleep problems. *JAMA Netw Open* 2023;**6**:e2348341.
33. Ouellette J, Toussay X, Comin CH, Costa LDF, Ho M, Lacalle-Aurioles M, et al. Vascular contributions to 16p11.2 deletion autism syndrome modeled in mice. *Nat Neurosci* 2020;**23**:1090−101.
34. Chen CJ, Sgritta M, Mays J, Zhou H, Lucero R, Park J, et al. Therapeutic inhibition of mTORC2 rescues the behavioral and neurophysiological abnormalities associated with Pten-deficiency. *Nat Med* 2019;**25**:1684−90.
35. Sato M, Nakai N, Fujima S, Choe KY, Takumi T. Social circuits and their dysfunction in autism spectrum disorder. *Mol Psychiatr* 2023;**28**:3194−206.
36. Crespo-Garcia M, Wang Y, Jiang M, Anderson MC, Lei X. Anterior cingulate cortex signals the need to control intrusive thoughts during motivated forgetting. *J Neurosci* 2022;**42**:4342−59.
37. Zhou C, Zhou Z, Han Y, Lei Z, Li L, Montardy Q, et al. Activation of parvalbumin interneurons in anterior cingulate cortex impairs observational fear. *Sci Bull* 2018;**63**:771−8.
38. Apps MA, Rushworth MF, Chang SW. The anterior cingulate gyrus and social cognition: tracking the motivation of others. *Neuron* 2016;**90**:692−707.
39. Bian XL, Qin C, Cai CY, Zhou Y, Tao Y, Lin YH, et al. Anterior cingulate cortex to ventral hippocampus circuit mediates contextual fear generalization. *J Neurosci* 2019;**39**:5728−39.
40. Yadav N, Noble C, Niemeyer JE, Terceros A, Victor J, Liston C, et al. Prefrontal feature representations drive memory recall. *Nature* 2022;**608**:153−60.
41. Paolicelli RC, Sierra A, Stevens B, Tremblay ME, Aguzzi A, Ajami B, et al. Microglia states and nomenclature: a field at its crossroads. *Neuron* 2022;**110**:3458−83.
42. Davalos D, Grutzendler J, Yang G, Kim JV, Zuo Y, Jung S, et al. ATP mediates rapid microglial response to local brain injury *in vivo*. *Nat Neurosci* 2005;**8**:752−8.
43. Nimmerjahn A, Kirchhoff F, Helmchen F. Resting microglial cells are highly dynamic surveillants of brain parenchyma *in vivo*. *Science* 2005;**308**:1314−8.
44. Hanisch UK, Kettenmann H. Microglia: active sensor and versatile effector cells in the normal and pathologic brain. *Nat Neurosci* 2007;**10**:1387−94.
45. Tong X, Ao Y, Faas GC, Nwaobi SE, Xu J, Haustein MD, et al. Astrocyte Kir4.1 ion channel deficits contribute to neuronal dysfunction in Huntington's disease model mice. *Nat Neurosci* 2014;**17**:694−703.
46. Chang SW, Gariepy JF, Platt ML. Neuronal reference frames for social decisions in primate frontal cortex. *Nat Neurosci* 2013;**16**:243−50.
47. Okamoto K, Hitora-Imamura N, Hioki H, Ikegaya Y. GABAergic malfunction in the anterior cingulate cortex underlying maternal immune activation-induced social deficits. *J Neuroimmunol* 2018;**321**:92−6.
48. Smith CJ, Kingsbury MA, Dziabis JE, Hanamsagar R, Malacon KE, Tran JN, et al. Neonatal immune challenge induces female-specific changes in social behavior and somatostatin cell number. *Brain Behav Immun* 2020;**90**:332−45.
49. Subramanian D, Eisenberg C, Huang A, Baek J, Naveed H, Komatireddy S, et al. Dysregulation of neuropilin-2 expression in inhibitory neurons impairs hippocampal circuit development and enhances risk for autism-related behaviors and seizures. *Mol Psychiatr* 2025;**30**:2799−809.
50. Zhao Y, Geng J, Meng Z, Sun Y, Ou M, Xu L, et al. Neurexin facilitates glycosylation of dystroglycan to sustain muscle architecture and function in Drosophila. *Commun Biol* 2024;**7**:1481.
51. Chowdhury TA, Luy DA, Scapellato G, Farache D, Lee ASY, Quinn CC. Ortholog of autism candidate gene *RBM27* regulates mitoribosomal assembly factor MALS-1 to protect against mitochondrial dysfunction and axon degeneration during neurodevelopment. *PLoS Biol* 2024;**22**:e3002876.
52. Cowen MH, Haskell D, Zoga K, Reddy KC, Chalasani SH, Hart MP. Conserved autism-associated genes tune social feeding behavior in *C. elegans*. *Nat Commun* 2024;**15**:9301.
53. Edmonson C, Ziats MN, Rennert OM. Altered glial marker expression in autistic post-mortem prefrontal cortex and cerebellum. *Mol Autism* 2014;**5**:3.
54. Bronzuoli MR, Facchinetti R, Ingrassia D, Sarvadio M, Schiavi S, Steardo L, et al. Neuroglia in the autistic brain: evidence from a preclinical model. *Mol Autism* 2018;**9**:66.
55. Varma M, Bhandari R, Sarkar A, Jain M, Paliwal JK, Medhi B, et al. Exploring astrocytes involvement and glutamate induced neuroinflammation in chlorpyrifos-induced paradigm of autism spectrum disorders (ASD). *Neurochem Res* 2024;**49**:2573−99.
56. Davoudi S, Rahdar M, Hosseinmardi N, Behzadi G, Janahmadi M. Chronic inhibition of astrocytic aquaporin-4 induces autistic-like behavior in control rat offspring similar to maternal exposure to valproic acid. *Physiol Behav* 2023;**269**:114286.
57. McColl ER, Piquette-Miller M. Poly(I:C) alters placental and fetal brain amino acid transport in a rat model of maternal immune activation. *Am J Reprod Immunol* 2019;**81**:e13115.
58. Chavez CE, Oyarzun JE, Avendano BC, Mellado LA, Inostroza CA, Alvear TF, et al. The opening of connexin 43 hemichannels alters hippocampal astrocyte function and neuronal survival in prenatally LPS-exposed adult offspring. *Front Cell Neurosci* 2019;**13**:460.
59. Manville RW, Block SD, Illeck CL, Kottmeier J, Sidlow R, Abbott GW. A novel autism-associated KCNB1 mutation dramatically slows K_V2.1 potassium channel activation, deactivation and inactivation. *Front Cell Neurosci* 2024;**18**:1438101.
60. Lauber E, Filice F, Schwaller B. Prenatal valproate exposure differentially affects parvalbumin-expressing neurons and related circuits in the cortex and striatum of mice. *Front Mol Neurosci* 2016;**9**:150.

61. Um KB, Kwak S, Cheon SH, Kim J, Hwang SK. AST-001 improves social deficits and restores dopamine neuron activity in a mouse model of autism. *Biomedicines* 2023;**11**:3283.
62. Cucchiara F, Frumento P, Banfi T, Sesso G, Di Galante M, D'Ascanio P, et al. Electrophysiological features of sleep in children with Kir4.1 channel mutations and autism-epilepsy phenotype: a preliminary study. *Sleep* 2020;**43**. zsz255.
63. Sicca F, Imbrici P, D'Adamo MC, Moro F, Bonatti F, Brovedani P, et al. Autism with seizures and intellectual disability: possible causative role of gain-of-function of the inwardly-rectifying K^+ channel Kir4.1. *Neurobiol Dis* 2011;**43**:239−47.
64. Sun C, Zou M, Li L, Li D, Ma Y, Xia W, et al. Association study between inwardly rectifying potassium channels 2.1 and 4.1 and autism spectrum disorders. *Life Sci* 2018;**213**:183−9.
65. Sicca F, Ambrosini E, Marchese M, Sforna L, Servettini I, Valvo G, et al. Gain-of-function defects of astrocytic Kir4.1 channels in children with autism spectrum disorders and epilepsy. *Sci Rep* 2016;**6**:34325.
66. Cui Y, Yang Y, Ni Z, Dong Y, Cai G, Foncelle A, et al. Astroglial Kir4.1 in the lateral habenula drives neuronal bursts in depression. *Nature* 2018;**554**:323−7.
67. Xie Y, Kuan AT, Wang W, Herbert ZT, Mosto O, Olukoya O, et al. Astrocyte−neuron crosstalk through Hedgehog signaling mediates cortical synapse development. *Cell Rep* 2022;**38**:110416.
68. Linnerbauer M, Wheeler MA, Quintana FJ. Astrocyte crosstalk in CNS inflammation. *Neuron* 2020;**108**:608−22.
69. Mondal R, Deb S, Chowdhury D, Sarkar S, Guha Roy A, Shome G, et al. Neurometabolic substrate transport across brain barriers in diabetes mellitus: implications for cognitive function and neurovascular health. *Neurosci Lett* 2024;**843**:138028.
70. Rangel-Gomez M, Alberini CM, Deneen B, Drummond GT, Manninen T, Sur M, et al. Neuron−glial interactions: implications for plasticity, behavior, and cognition. *J Neurosci* 2024;**44**: e1231242024.
71. Meng X, Wu W, Tang Y, Peng M, Yang J, Yuan S, et al. Lactate/-hydroxycarboxylic acid receptor 1 in Alzheimer's disease: mechanisms and therapeutic implications-exercise perspective. *Mol Neurobiol* 2024;**61**:7717−31.
72. Klambt C. Modes and regulation of glial migration in vertebrates and invertebrates. *Nat Rev Neurosci* 2009;**10**:769−79.
73. Calderoni S. Sex/gender differences in children with autism spectrum disorder: a brief overview on epidemiology, symptom profile, and neuroanatomy. *J Neurosci Res* 2023;**101**:739−50.
74. Napolitano A, Schiavi S, La Rosa P, Rossi-Espagnet MC, Petrillo S, Bottino F, et al. Sex differences in autism spectrum disorder: diagnostic, neurobiological, and behavioral features. *Front Psychiatr* 2022; **13**:889636.